

Bag of Design Choices for Inference of High-Resolution Masked Generative Transformer

Shitong Shao¹ Zikai Zhou^{1,◇} Tian Ye¹ Lichen Bai¹ Zhiqiang Xu² Zeke Xie^{1,*}

¹Hong Kong University of Science and Technology (Guangzhou)

²Mohamed bin Zayed University of Artificial Intelligence

{sshao213, zikaizhou, lichenbai, zekexie}@hkust-gz.edu.cn

tye610@connect.hkust-gz.edu.cn zhiqiang.xu@mbzuai.ac.ae

◇:Equal Contribution

*:Corresponding author

Abstract

Text-to-image diffusion models (DMs) develop at an unprecedented pace, supported by thorough theoretical exploration and empirical analysis. Unfortunately, the discrepancy between DMs and autoregressive models (ARMs) complicates the path toward achieving the goal of unified vision and language generation. Recently, the masked generative Transformer (MGT) serves as a promising intermediary between DM and ARM by predicting randomly masked image tokens (i.e., masked image modeling), combining the efficiency of DM with the discrete token nature of ARM. However, we find that the comprehensive analyses regarding the inference for MGT are virtually non-existent, and thus we aim to present positive design choices to fill this gap. We modify and re-design a set of DM-based inference techniques for MGT and further elucidate their performance on MGT. We also discuss the approach to correcting token’s distribution to enhance inference. Extensive experiments and empirical analyses lead to concrete and effective design choices, and these design choices can be merged to achieve further performance gains. For instance, in terms of enhanced inference, we achieve winning rates of approximately 70% compared to vanilla sampling on HPS v2 with the recent SOTA MGT Meissonic. Our contributions have the potential to further enhance the capabilities and future development of MGTs.

1. Introduction

The rapid development of generative models has successfully sparked a deep learning innovations in both computer vision and natural language processing. The emergence of large language models (LLMs) in natural language processing, along with their strong generalization across domains and tasks [27, 43, 46], benefits from the autoregressive

model (ARM) with the Transformer decoder block [52]. By contrast, the dominant paradigm in text-to-image (T2I) synthesis is the diffusion model (DM), which employs a multi-step denoising process to synthesize high-quality images from Gaussian noise [12, 20, 35–37, 39]. The significant variability in training and inference between ARMs and DMs hinders the unification of generative paradigms in computer vision and natural language processing. The recent accomplishments of some ARMs in visual generation, such as LlamaGen [42], Lumina-mGPT [21], and Fluid [8], indicates that DMs are not the sole option for achieving success in image generation. This paradigm synthesizes extremely high-quality images but requires hundreds or even thousands of function evaluations (NFEs) to synthesize a single image [44]. Instead, masked generative Transformers (MGTs) [5] predict multiple masked tokens in each forward pass, resulting a trade-off between DMs and ARMs. This approach preserves the efficiency of DMs while stabilizing the transformation of images into discrete tokens, thus aligning with the part characterization of LLM [34].

A recent MGT, Meissonic [3], achieved high-quality image synthesis at the 1024×1024 resolution for the first time, setting a new state-of-the-art performance on HPS v2 [49] and outperforming SD XL [29] by a margin of 0.69. This phenomenon substantiates MGT’s capability to synthesize high-resolution images and suggests the potential for developing a commercial-grade generative model, such as FLUX [16]. Unfortunately, compared to the extensive theoretical research and empirical analysis in the DM field, scholarly exploration and understanding of high-resolution MGTs remain unexplored, hindering the further development of MGT in both training and inference [3, 5, 6].

To fill this gap, this paper focuses on the inference phase of MGT, aiming to identify effective design choices for enhancing visual quality and achieving efficient sampling using empirical analysis in high-resolution image synthesis

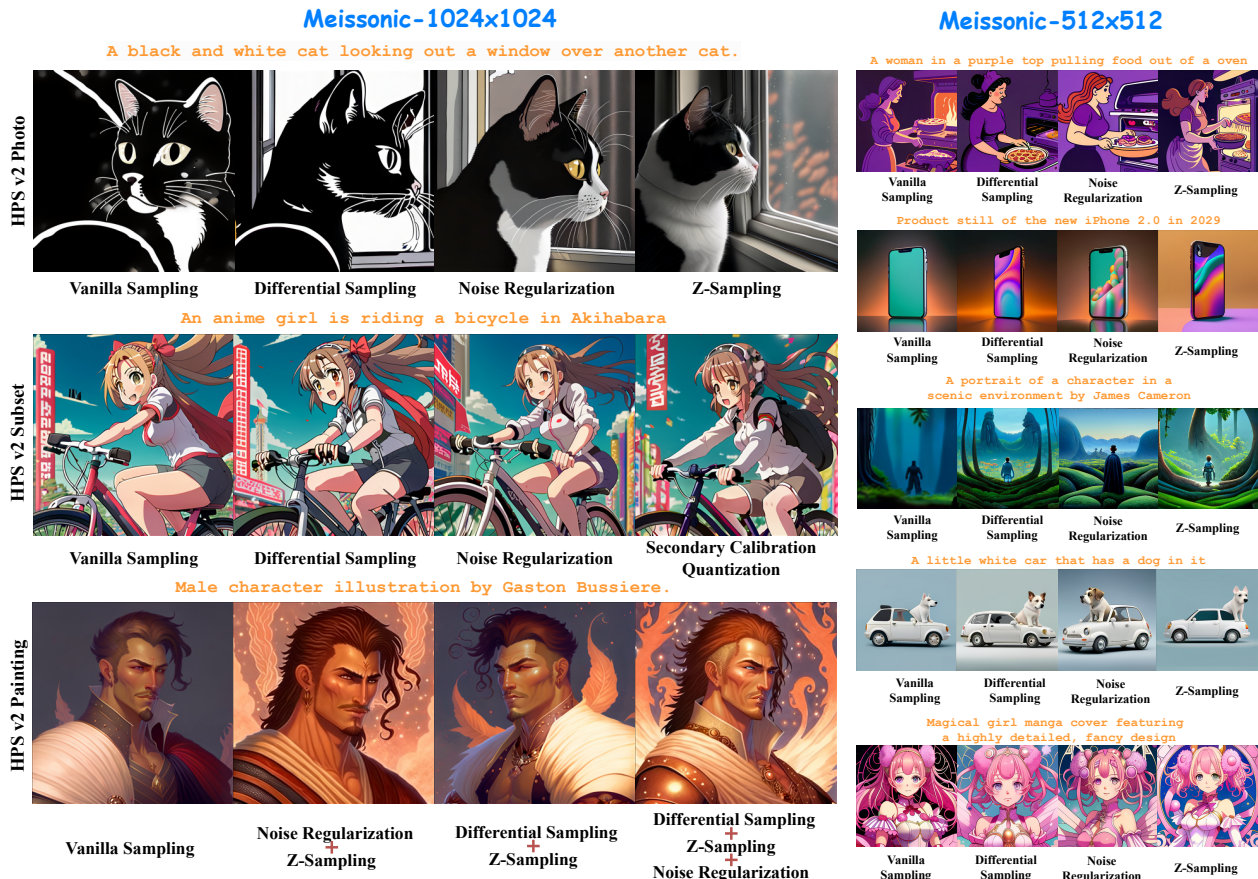


Figure 1. Visualization of our design choices on Meisssonic-512 \times 512 and Meisssonic-1024 \times 1024. Noise regularization, differential sampling, and Z-Sampling significantly improve both visual quality and semantic faithfulness. Additionally, our quantization method secondary calibration quantization (SCQ) can reduce the memory footprint without significant performance degradation.

scenarios. *First*, we elucidate how well-known training-free methods in DM can be applied to MGT, and the redesign required to ensure their effectiveness. As illustrated in Fig. 2 and Table 1, the sampling process of MGT bears significant similarity to that of DM, making it intuitive to adapt those algorithms from DM to MGT. We explore DPM-Solver [23, 24], TomeSD [4], and Z-Sampling [2] in this context, but find that all three algorithms require specific modifications to align with the characteristics of MGT in order to reduce NFE, accelerate inference, or achieve performance improvements. Given an example of Z-Sampling, we find that implementing DDIM Inversion [26], as used in DM, with random masking is ineffective unless masking is limited to low-confidence predicted tokens. In particular, our experimental outcomes indicate that among these three algorithms, DPM-Solver and TomeSD have relatively limited effects on MGT, whereas a rescheduling algorithm like Z-Sampling yields notable performance gains. Furthermore, we investigate the noise schedule in MGT, akin to EDM [14], highlighting that the cosine noise schedule is suboptimal under certain conditions. These findings suggest that inconsistencies between the training and inference

mechanisms of DM and MGT lead to enhanced inference algorithms on DM not necessarily being effective for MGT.

Second, we take a look at the probability distribution generated by the backbone (*i.e.*, Transformer), leading to the development of several “cheap” (*i.e.*, w/o significant computational overhead) yet effective distribution correction algorithms, including noise regularization and (low-entropy) differential sampling. To be specific, noise regularization dynamically applies (Gaussian) perturbations to the backbone output based on timesteps before applying *softmax*, aiming to enhance the diversity of synthesized images. Differential sampling, on the other hand, calculates the Kullback-Leibler (KL) divergence between the outputs of two adjacent time steps and resamples tokens with excessively similar Transformer outputs, thereby avoiding information redundancy and enhancing the visual quality.

Third, we also investigate the model quantization on Meisssonic for efficient memory usage. Our results reveal that Weight4Activation16 (W4A16) quantization fails to reduce memory usage in practice, while W4A8 quantization results in inference collapse. To address this issue, we quantize only the layers with low-amplitude activation values,

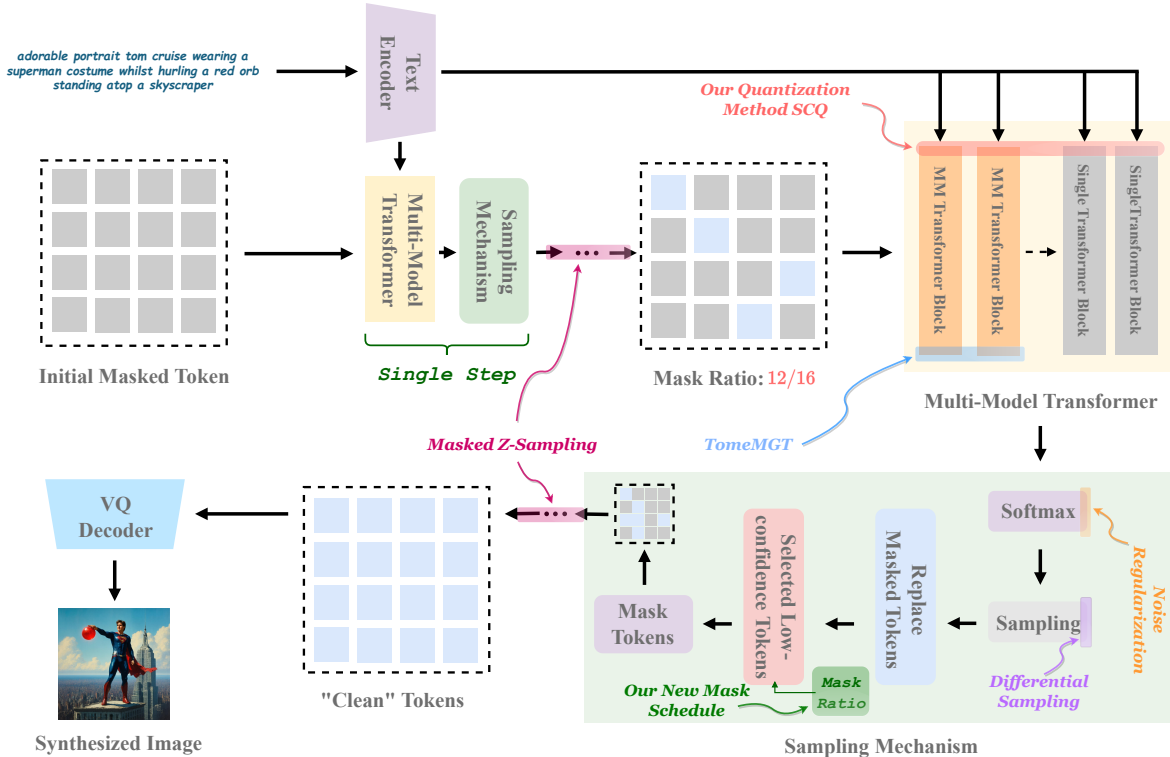


Figure 2. The complete sampling pipeline of MaskGIT, Muse, and Meissonic, and how our proposed effective and specific design choices integrate into that sampling pipeline. Specifically, TomeMGT and SCQ act on the multi-model (MM) Transformer to reduce inference latency and memory usage, respectively. Meanwhile, noise regularization and differential sampling enhance inference by correcting the probability distribution applied for sampling. Additionally, masked Z-Sampling is a rescheduling technique that significantly improves the quality of synthesized images through the forward-inversion operator (*i.e.*, sampling and backtracking alternatively).

reducing the memory footprint from 11.98 GB to 4.57 GB w/o significant performance degradation.

Fourth, we validate the effectiveness of our proposed design choices on the HPD v2 benchmark using various metrics, including ImageReward [50], HPS v2 [48], PickScore [10, 19], and AES [17]. As illustrated in Fig. 1, these strategies significantly improve the visual quality of synthesized images. Furthermore, we introduce Challengebench, which includes 220 prompts to evaluate the robustness of Meissonic [3] on challenging cases. The results demonstrate that Meissonic shows a greater performance gain on Challengebench compared to SD XL [29], as opposed to the HPD v2 benchmark.

2. Preliminaries

We begin by reviewing three generative models that are experiencing continuous growth in the field of vision synthesis: diffusion model (DM) [12], autoregressive model (ARM) [42], and masked generative Transformer (MGT) [3]. We then provide an overview of MGT’s vanilla sampling process, which is introduced by MaskGIT [5].

Inference Mechanism of Visual Generative Model. DM is a well-established technique that has developed in recent years and has successfully scaled to large-scale, high-

quality visual synthesis, whereas ARM [21] and MGT [3] have only recently demonstrated feasibility for synthesizing high-resolution images. As illustrated in Table 1, each of them employs the multi-step denoising paradigm to progressively generate high-quality images during inference. Given a latent variable \mathbf{z}_{t_0} (t is defined in Table 1), it may follow a Gaussian distribution (*w.r.t.*, DM) or consist of masked tokens (*w.r.t.*, ARM and MGT). These methods primarily expect to fit the (abstract) estimator $p(\mathbf{z}_{t_i}|\mathbf{z}_{t_{i-1}})$ ($i \geq 1$) in the training phase, thus enabling the sequential sampling $p(\mathbf{z}_{t_N}|\prod_{i=0}^{N-1} \mathbf{z}_{t_i}) = p(\mathbf{z}_{t_0})\prod_{i=1}^N p(\mathbf{z}_{t_i}|\mathbf{z}_{t_{i-1}})$ during inference, where N stands for the number of sampling steps. Note that $p(\mathbf{z}_{t_i}|\mathbf{z}_{t_{i-1}})$ can be instantiated in various models with distinct focuses: in DM, it represents the prediction of a score function; in ARM, it embodies the prediction of a token; and in MGT, it pertains to the prediction of all masked tokens. In both DM and MGT, the encoder-only Transformer is employed to predict the complete score function or the full tokens, allowing their sampling process to be refined as $p(\mathbf{z}_{t_i}|\mathbf{z}_{t_{i-1}}) = \int_{\mathbf{z}_{t_N}} p(\mathbf{z}_{t_i}|\mathbf{z}_{t_{i-1}}, \mathbf{z}_{t_N})p(\mathbf{z}_{t_N}|\mathbf{z}_{t_{i-1}})d\mathbf{z}_{t_N}$.

Vanilla Sampling Process of MGT. The sampling process for MGT was given by MaskGIT [5] and subsequently followed by Muse [6] and Meissonic [3]. As illustrated in

Table 1. Specific design choices employed by masked generative Transformers (MGTs) are presented in this overview. We adopt a definitional form of sampling that is consistent with DMs, akin to EDM [14]. Let N denote the number of sampling steps, and the sequence of time steps is $\{t_0, \dots, t_N\}$, where $\sigma_{t_N} = 0$. Furthermore, the strategies highlighted in yellow are our proposed methods.

	DM [39]	ARM [42]	MGT [3]	Ours
Definition (Section 2)				
TimeStep	$t_{0 \leq i < N}$ $t = 1 + \frac{i}{N}(\epsilon - 1)$ (VP-SDE & flow matching) i/N (EDM)	N/A (next-token prediction)	i/N (non-ar token prediction)	i/N (non-ar token prediction)
Noise Schedule (Section 3.1)	σ_t $\sqrt{e^{a^2 t + bt} - 1}$ (VP-SDE [39]) t (flow matching [22]) $(\sigma_{\max}^{\frac{1}{2}} + t(\sigma_{\min}^{\frac{1}{2}} - \sigma_{\max}^{\frac{1}{2}}))^{\rho}$ (EDM [14])	N/A, and predicts one token per iteration	$\cos\left(\frac{\pi t}{2}\right)$	$(1-t)^{\rho}$ or $1-t^{\rho}$
Network Architecture	f_{θ} U-Net [12] or Transformer [28] (encoder only)	Transformer [42] (decoder only)	Transformer [3] (encoder only)	Transformer [3] (encoder only)
Coding Form	$Q(z x)$ VAE [15] (continuous)	VQ-VAE [47] (discrete)	VQ-VAE [47] (discrete)	VQ-VAE [47] (discrete)
Enhanced Inference (Section 3)				
Sampling Paradigm $p(z_i \prod_{j < i} z_j)$ (Sec. 3.2)	DDPM [12], Euler Maruyama [39], Classifier-free Guidance [11], Z-Sampling [2], et al.	Autoregressive (z_i denotes a token)	MaskGIT’s Sampling [5] (z_i denotes all masked tokens)	Masked Z-Sampling, i.e. $p(z_i \bar{z}_i, \prod_{j < i} z_j)$, where $\bar{z}_i \sim p(z_i \prod_{j < i} z_j)$ (z_i denotes all masked tokens)
Improved Probability Distribution (Sec. 3.3 & 3.4)	N/A	$\arg \max_i \frac{\log(\epsilon)}{p}$, where p is the logit and $\epsilon \sim \mathcal{U}[0, 1]$	$\arg \max_i \frac{\log(\epsilon)}{p}$, where p is the logit and $\epsilon \sim \mathcal{U}[0, 1]$	Noise regularization and differential sampling
Efficient Inference (Section 4)				
Quantization (Section 4.1)	Both Int4 and Int8 have been successfully [7]	N/A	N/A	W4A8 Quantization (Our proposed SCQ)
Token Merging (Section 4.2)	TomeSD [4]	N/A	N/A	TomeMGT (Transfer TomeSD into MGT)
Reduce NFE (Section 4.3)	DDIM [37], Deis [51] and DPM-Solver [24]	Jacobi Decoding [45]	N/A	Momentum-based Solver
W4A8: the weights are quantized to 4 bits and the activation values are quantized to 8 bits.			$a, b, \sigma_{\max}, \sigma_{\min}: 9.95, 0.1, 80, 0.002.$	

Fig. 2, the complete sampling process of MGT closely resembles counterpart of DM, though they differ in several critical aspects. To be specific, given the initial masked tokens z_{t_0} , it is sampled in multiple steps to obtain the “clean” tokens z_{t_N} . Taking Meissonic as an example, each step i involves: 1) the MM Transformer giving the predicted tokens; 2) replacing the masked tokens in z_{t_i} with the predicted tokens, followed by masking out tokens with low confidence based on their probability values. The main differences between the sampling processes of MGT and DM are: 1) each step of MGT is modeled non-deterministically (see Table 1), and forcing deterministic sampling is likely to degrade performance (see Appendix 8.1 for details); 2) in MGT, the predicted tokens only replace the masked tokens and do not affect the unmasked tokens; and 3) how the masking is performed in MGT is determined by probability values, unlike DM, which is random.

3. Enhanced Inference

Sec. 3 and Sec. 4 will discuss our explorations of enhanced and efficient inference, respectively. In this section, enhanced inference involves adaptations of well-known DM methods, along with new algorithms designed based on the properties of MGT. Note that to introduce our research more logically, we will introduce our methods and experiments in the form of a progressive exploration. For follow-up content, we employ the definitions in Table 1. All experiments,

unless otherwise specified, were conducted with Meissonic-1024×1024 on the HPD v2 Subset (see Appendix 7).

3.1. Convexity Exploration of Noise Schedule

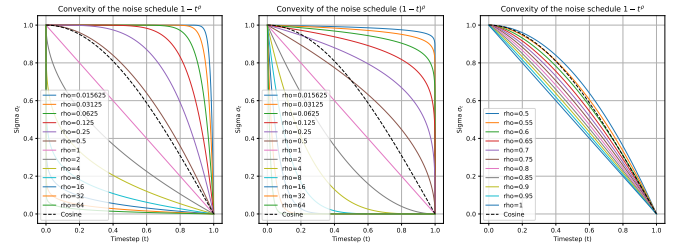


Figure 3. Visualization of different noise schedules. The black dashed line represents the cosine schedule.

All known MGT models use the cosine schedule shown in Table 1 for both training and inference to ensure consistency. To investigate whether a better noise schedule exists for inference, we explore curves with different convexities (see Fig. 3). The curve design is inspired by Karras’ noise schedule [14]. Specifically, the expressions $(\sigma_{\begin{smallmatrix} \text{begin} \\ \text{end} \end{smallmatrix}}^{\frac{1}{\rho}} + t(\sigma_{\text{end}}^{\frac{1}{\rho}} - \sigma_{\begin{smallmatrix} \text{begin} \\ \text{end} \end{smallmatrix}}^{\frac{1}{\rho}}))^{\rho}$ and $1 - ((1 - \sigma_{\begin{smallmatrix} \text{begin} \\ \text{end} \end{smallmatrix}})^{\frac{1}{\rho}} + t((1 - \sigma_{\text{end}})^{\frac{1}{\rho}} - (1 - \sigma_{\begin{smallmatrix} \text{begin} \\ \text{end} \end{smallmatrix}})^{\frac{1}{\rho}}))^{\rho}$ can be simplified to $(1-t)^{\rho}$ and $1-t^{\rho}$ when $\sigma_{\begin{smallmatrix} \text{begin} \\ \text{end} \end{smallmatrix}}$ is set to 1 and σ_{end} to 0. We present the experimental results in Fig. 4 and Table 2, where the number of sampling steps N is set to 64.

The key takeaway from Fig. 4 is that $1-t^{\rho}$ outperforms

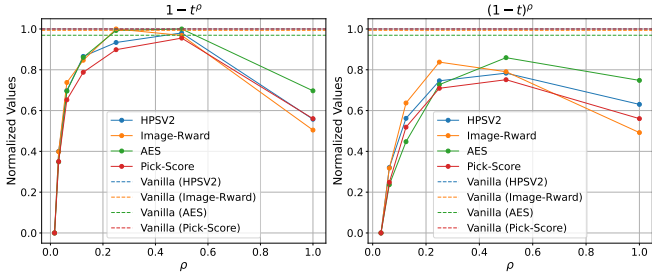


Figure 4. Visualization of the performance of different noise schedules. The dotted line denotes the vanilla sampling.

$(1-t)^\rho$, with the most metrics peaking around $\rho = 0.5$. Notably, some metrics even exceed the performance of vanilla sampling. Given this observation, we sample ρ more densely and uniformly within the interval $[0.5, 1]$ to obtain more precise results, which is presented in Table 2.

Method	HPS v2 (\uparrow)	ImageReward (\uparrow)	AES (\uparrow)	PickScore (\uparrow)
Cosine Schedule	0.3062	1.0627	6.1938	22.5037
$1-t^\rho$ ($\rho = 1$)	0.2835	0.7679	6.0017	21.8594
$1-t^\rho$ ($\rho = 0.95$)	0.2866	0.8160	6.0652	21.9837
$1-t^\rho$ ($\rho = 0.9$)	0.2914	0.8647	6.0632	22.1004
$1-t^\rho$ ($\rho = 0.85$)	0.2939	0.9500	6.1004	22.2132
$1-t^\rho$ ($\rho = 0.8$)	0.2974	0.9728	6.1094	22.3202
$1-t^\rho$ ($\rho = 0.75$)	0.3011	1.0323	6.1785	22.3804
$1-t^\rho$ ($\rho = 0.7$)	0.3019	1.0407	6.1734	22.4451
$1-t^\rho$ ($\rho = 0.65$)	0.3051	1.0153	6.1945	22.4474
$1-t^\rho$ ($\rho = 0.6$)	0.3080	1.0889	6.2101	22.5380
$1-t^\rho$ ($\rho = 0.55$)	0.3051	1.0520	6.2351	22.4428
$1-t^\rho$ ($\rho = 0.5$)	0.3052	1.0476	6.2155	22.4381

Table 2. Comparison between cosine schedule and $1-t^\rho$.

When $\rho = 0.6$, $1-t^\rho$ demonstrates more favorable behavior compared to the standard cosine schedule $\cos(\frac{\pi t}{2})$. This substantiates that, even if the cosine schedule is used during training, a better noise schedule may exist for inference. We also present additional experimental results for different values of N and benchmarks in Appendix 9.1.

3.2. Masked Z-Sampling for MGT

The core idea of Zigzag diffusion sampling (Z-Sampling) [2, 25] is to improve the sampling quality of DMs by incorporating “future” semantic information in advance, using a “zigzag” path for sampling. We aim to extend this algorithm, which has demonstrated effective for DMs, to MGT to enhance the fidelity of synthesized images. The logic of Z-Sampling is illustrated by the equation at the top of Fig. 5. After obtaining the latent \hat{z}_i , it backtracks to $t=i-1$ using the “specific” masking algorithm (corresponds to DDIM Inversion in DMs) and performs sampling from $t=i-1$ to $t=i$ again.

Unfortunately, applying random masking (*i.e.*, vanilla Z-Sampling in Fig. 5) to simulate DDIM inversion in DMs impaired inference performance in our experiments. We argue that this is due to random masking incorrectly removing certain tokens in the latent space that significantly contribute to the synthesized image. For instance, the purple

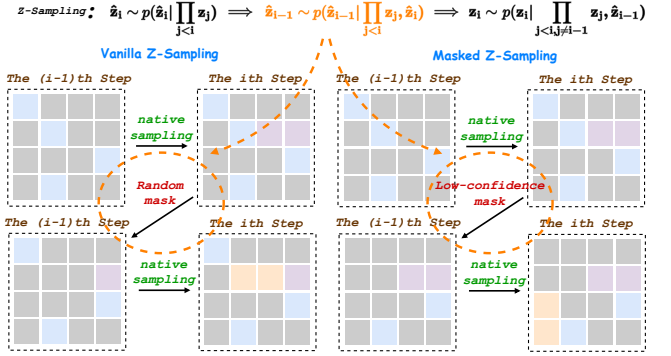


Figure 5. The illustration of vanilla Z-Sampling and masked Z-Sampling. The main difference is the masking form.

token obtained during the 1st forward sampling in Fig. 5 may be masked out, even though these purple tokens typically represent the most “future” information. Therefore, we employ a novel masking pipeline for backtracking that is consistent with that of sampling mechanism, specifically masking the portion of the predicted token at the i th step with the low log probability (*i.e.*, masked Z-Sampling in Fig. 5). We also need to mention an important parameter: the inversion classifier-free guidance (CFG) scale, which refers to the CFG scale used to generate tokens for selecting low-confidence probabilities during the masking phase. We looked at how the inversion CFG scale affect the quality of synthesized images. As outlined in [2] that a “just right” CFG gap can be produced by selecting a desirable inversion CFG scale that maximizes the positive impact of semantic information injection.

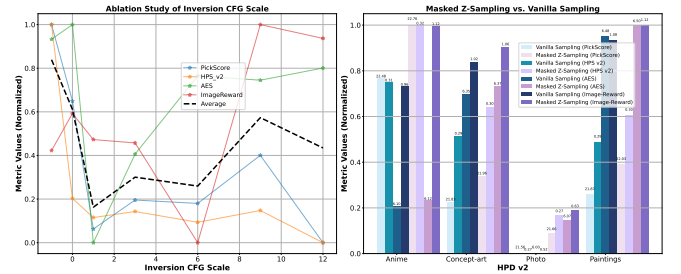


Figure 6. **Left:** Ablation study on the inversion CFG scale. **Right:** Comparison between masked Z-Sampling and vanilla sampling on the HPD v2 dataset.

We present the ablation results in Fig. 6 (Left). From the change in the black dashed line (*i.e.*, average metric), it can be concluded that the inversion CFG scale performs best near -1 and 9. To reduce computational cost, we set the inversion CFG scale to 0 (*i.e.*, do not use CFG) and the standard CFG scale to 9 in our experiments, thereby avoiding additional computational overhead by reducing the NFE.

We further validate masked Z-Sampling on the HPD v2 dataset, with the results presented on Fig. 6 (Right). It can be observed that our algorithm significantly outperforms vanilla sampling across nearly all domains and metrics,

demonstrates that masked Z-Sampling can steadily enhance the performance of MGT.

3.3. Noise Regularization

According to our research, a major difference between MGT and DMs is that MGT can improve the visual quality and diversity of synthesized images by adjusting the model outputs’ probability distribution. As a result, noise regularization and differential sampling are proposed. Here, we first present a simple yet effective approach known as noise regularization, which can be described as

$$\begin{aligned} \mathbf{v}_i &= f_\theta(\mathbf{z}_i, t_i), \\ \hat{\mathbf{v}}_i &= \mathbf{v}_i + \epsilon_t, \text{ where } \epsilon_t \sim \mathcal{N}(\mathbf{0}, \mathbf{I}_t), \\ \mathbf{p}_i &= \text{softmax}(\hat{\mathbf{v}}_i), \end{aligned} \quad (1)$$

where \mathbf{v}_i is the output of f_θ and the yellow part stands for noise regularization. As shown in Fig. 7 (Left), vanilla sampling often results in horizontal bars of the same color as t approaches 0 and vertical bars of the same color as t approaches 1, indicating the redundancy of its sampling process. Noise regularization introduces randomness into the sampling process, eliminating color bars of the same color and thereby enhancing the diversity of predicted tokens.

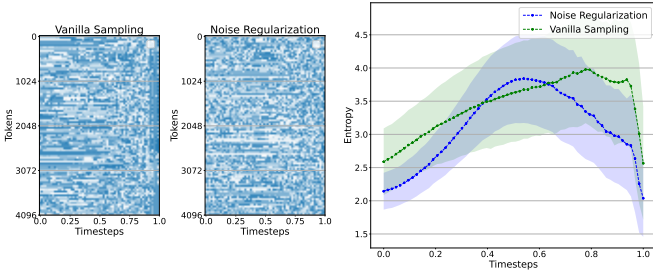


Figure 7. **Left:** The sampling trajectory of noise regularization. Different colored tokens represent different values $\in \{0, \dots, 8191\}$. **Right:** The visualization of the entropy as the sampling progresses. Shaded blocks are the standard deviations.

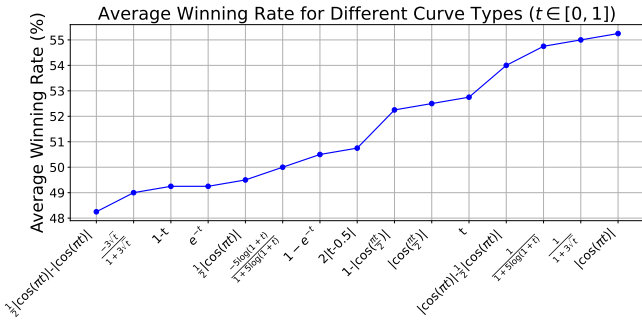


Figure 8. Ablation study on $\mathbf{I}(t)$. Note that $\frac{1}{2}|\cos(\pi t)| - |\cos(\pi t)|$ and $|\cos(\pi t)| - \frac{1}{2}|\cos(\pi t)|$ represent the scenarios where the function $\frac{1}{2}|\cos(\pi t)|$ or $|\cos(\pi t)|$ is used for $t \in [0, \frac{1}{2})$, while $|\cos(\pi t)|$ or $\frac{1}{2}|\cos(\pi t)|$ is used for $t \in [\frac{1}{2}, 1]$, respectively.

In our definition, the hyperparameter \mathbf{I}_t is a function $\mathbf{I}(t)$ that varies dynamically with t . To empirically determine the

empirically optimal $\mathbf{I}(t)$, we test various curves and calculate the winnowing rates of four metrics—PickScore, HPS v2, AES, and ImageReward—relative to vanilla sampling. The results are presented in Fig. 8. We find that $\mathbf{I}(t)$ works best when set to $|\cos(\pi t)|$, which reaches larger values as t approaches 0 or 1 and lower values in the middle. This observation is interesting, as injecting noise during the end-of-sampling phase significantly degrades inference performance on DM, while having positive impact on MGT. Additionally, as presented in Fig. 7 (Right), noise regularization modifies the entropy of the distribution during the sampling phase, making it more inclined toward a “U”-shaped structure, which is similar to the shape of $|\cos(\pi t)|$. The results on HPD v2 can be found in Appendix 9.3.

3.4. Differential Sampling

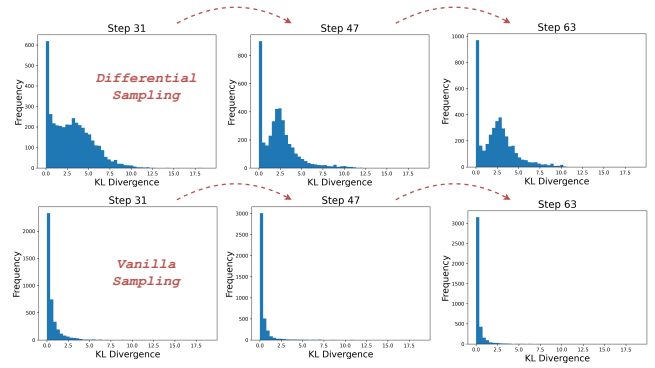


Figure 9. Trajectory of KL divergence between distributions at neighboring time steps throughout the sampling process. Note that the variability in the distributions of two consecutive steps in vanilla sampling is minimal as KL divergence are all close to 0.

The effectiveness of noise regularization highlights the importance of enhancing diversity in MGT by adjusting the probability distribution. In addition to this, we show in Fig. 9 (Bottom) that the probability distribution tends to overly rely on the outputs from certain timesteps, which leads to the propagation of similarity throughout the sampling process. In response to this issue, we propose (low-entropy) differential sampling, which resamples the probability distribution of the current step when it is too similar to that of the previous step. Assume that the probability distribution of the j th token at the i th step is denoted by \mathbf{p}_i^j ($i \geq 1$). The KL divergence between distributions at the i th step and the $(i-1)$ th step can then be expressed as

$$\mathcal{D}_i = \{d_i^1, d_i^2, \dots, d_i^K\}, \quad d_i^j = \mathcal{D}_{\text{KL}}(\mathbf{p}_i^j \| \mathbf{p}_{i-1}^j), \quad (2)$$

where \mathcal{D}_i , K and $\mathcal{D}_{\text{KL}}(\cdot \| \cdot)$ refer to the KL divergence set, the number of tokens, KL divergence, respectively. To identify the tokens with the worst propagation of similarity, we sort \mathcal{D}_i and reject the lowest $z\%$ of tokens and then resampling them, where the resampling comes from the differen-

tial between two probability distributions:

$$\tilde{p}_i^j = \frac{|p_i^j - p_{i-1}^j|}{\sum_{p \in |p_i^j - p_{i-1}^j|} p}. \quad (3)$$

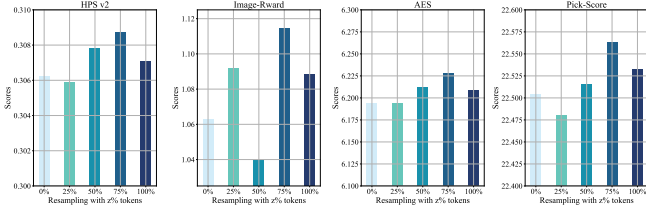


Figure 10. Ablation Studies of $z\%$ in differential sampling.

As shown in Fig. 9 (Top), this approach can significantly mitigate the propagation of similarity and effectively introduce diversity into the sampling process. Moreover, we conduct ablation experiments on the hyperparameter z , and the results are presented in Fig. 10. As z increases from 0 to 100 ($z=0$ means vanilla sampling), the sampling performance initially improves and then declines. Interestingly, differential sampling outperforms vanilla sampling even when applied to all tokens, highlighting the robustness of differential sampling. Furthermore, empirical results indicate that the best performance is achieved when z is set to 75., and we present the performance of differential sampling on HPD v2 in Appendix 9.4.

4. Efficient Inference

Another path we explore is determining how to achieve efficient inference on MGT. We consider model quantization [13], token merging [4], and scheduling strategies similar to those used in DM [23, 24, 30].

4.1. Secondary Calibration for Quantization

The most effective way to achieve memory efficiency is to apply model quantization to the backbone of generative model, a technique successfully used in FLUX [16] and SD 3.5 [40]. Unfortunately, this approach does not work on Meissonic-1024×1024 due to 1) its limited number of model parameters (only 1 billion) and its compression layer that actively reduces the number of tokens to 1024. These constraints lead to issues when applying W4A16 post-training quantization (PTQ), resulting in an inability to synthesize normal images. In addition, 2) since Meissonic incorporates a multi-model transformer block, the overly complex architectural design prevents the quantized memory from being significantly reduced in practice. A straightforward solution is to quantize the activation values. However, this operation further degrades model performance.

To address these issues, we propose secondary calibration for quantization (SCQ). Our core contribution involves 1) performing quantization-aware training (QAT) using Meissonic’s synthesized images to correct the range of

quantized values, followed by 2) introducing a secondary calibration strategy that records the magnitude of each layer after primary calibration and subsequently quantizes only the activation values with smaller magnitudes, further calibrating them. In our experiments, we quantized only one-third of the activation values by default, which reduced the backbone’s memory usage from 3.34 GB to 2.24 GB.

The experimental results of SCQ are presented in Table 3, where “A8W4-QAT & Calibration” represents a single calibration step performed on the Transformer (i.e., backbone) derived from QAT. For a fair comparison, one-third of the activation values were randomly selected for quantization in “A8W4-QAT & Calibration”. Additionally, “CPU offloading” indicates that the transformer was used first to obtain all z_N , after which the tokenizer decoder is loaded to transform z_N into synthesized images. From Table 3, it can be concluded that both QAT and secondary calibration strategies are critical and effective.

4.2. Introducing TomeSD into MGT

Applying token merging to accelerate inference is natural, as the backbone of MGT is a transformer. Unfortunately, Meissonic has only 1024 tokens, fewer than 4096 tokens in the attention layer of SD XL. As is well known, the computational complexity of attention increases exponentially with the number of tokens, and a smaller number of tokens reduces the potential benefits of token merging, resulting in an insignificant effect of our implemented TomeMGT as observed in our experiments. Therefore, we focus on the challenges of applying TomeSD, which has demonstrated effective on SD XL, to MGT to achieve accelerated inference, along with the corresponding application scenarios.

The main challenge consists of two aspects. *First*, applying token merging to a single transformer may cause inference to fail, whereas it is effective in a multi-modal transformer. *Second*, RoPE [41] (used for encoding positional information) in Meissonic also requires merging. For the former, we perform token merging only on multi-modal transformers, while for the latter, we provide details on our handling of RoPE in Appendix 9.5. Here, we present only the ablation studies on the merging ratio on Table 5. The comparison experiments are provided in Appendix 9.6.

4.3. Momentum-based Solver

Inspired by the success of DDIM [37] and DPM-Solver [24] in DM, we aim to implement a similar mechanism in MGT. Since the 1st order form of DPM-Solver is equivalent to DDIM, we focus on implementing DPM-Solver. We call our implementation of DPM-Solver in MGT Momentum-based Solver since these algorithms basically use momentum for accelerated sampling [32, 38, 53]. The analytical

Method	Total Memory Usage	Transformer Memory Usage	HPS v2 (\uparrow)	ImageReward (\uparrow)	AES (\uparrow)	PickScore (\uparrow)
Float32	11.98 GB	6.82 GB	0.3062	1.0627	6.1938	22.5037
Float16	9.55 GB	3.38 GB	0.3041	1.0019	6.1827	22.5333
Bfloat16	6.78 GB	3.34 GB	0.3069	1.0867	6.2222	22.4525
A8W4-PTQ	5.86 GB	2.24 GB	0.1009	-2.2533	4.1185	17.1369
A8W4-QAT & Calibration	5.86 GB	2.24 GB	0.3063	1.0055	6.1227	22.2648
A8W4-SCQ (ours)	5.86 GB	2.24 GB	0.3066	1.0635	6.1907	22.4406
A8W4-SCQ (CPU offloading, ours)	4.57 GB	2.24 GB	0.3066	1.0635	6.1907	22.4406

Table 3. Comparison of different quantization methods on HPD v2 Subset. Our proposed SCQ reduces total memory usage from 11.98 GB to 4.57 GB with minimal performance loss. All memory is recorded using `torch.cuda.max_memory_reserved()`.

Model	Method	HPS v2 (\uparrow)	ImageReward (\uparrow)	AES (\uparrow)	PickScore (\uparrow)
Meissonic	N/A	0.2116	0.0670	5.8503	19.3237
SD XL	N/A	0.1838	-0.4915	5.8195	19.5792
FLUX.1-schnell (quant 8bit)	N/A	0.2257	0.2595	6.0357	19.6465
SD-3.5-Large (quant 4bit)	N/A	0.2114	0.0373	6.0848	19.7922

Table 4. Comparison of various models on Challengebench. The result of our methods can be found in Appendix 9.8.

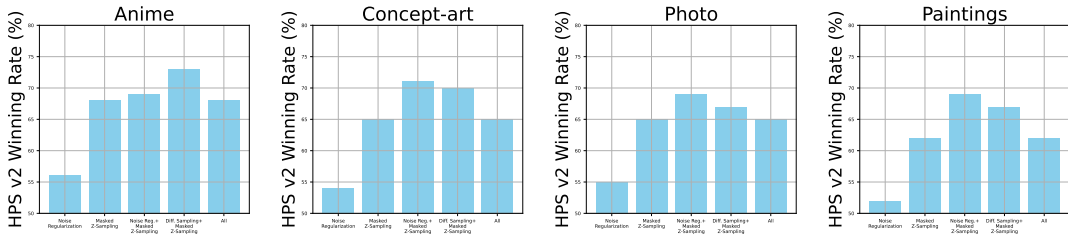


Figure 11. Comparison of the combination of our methods on HPD v2. The results for Meissonic-512x512 can be found in Appendix 9.9.

Merging Ratio	HPS v2	Image Reward	AES	PickScore	Time Spent (s/per img)
0%	0.3062	1.0627	6.1938	22.5037	8.38
25%	0.2976	0.9187	6.0479	22.1302	7.98
50%	0.2723	0.6365	5.8335	21.3290	7.97
75%	0.1182	-2.1480	4.1857	17.6813	7.90

Table 5. Ablation studies of merging ratio on a single RTX 4090.

equations of the 1st and 2nd orders can be written as

$$\begin{aligned}
 \mathbf{z}_t &= \frac{\sigma_t}{\sigma_s} \mathbf{z}_s - \frac{\sigma_t - \sigma_s}{\sigma_s} f_\theta(\mathbf{z}_s, \sigma_s), & \# \text{ 1st order} \\
 \mathbf{z}_t &= \frac{\sigma_t}{\sigma_s} \mathbf{z}_s - \frac{\sigma_t - \sigma_s}{\sigma_s} f_\theta(\mathbf{z}_s, \sigma_s) + & \# \text{ 2nd order} \\
 & ((\sigma_t - \sigma_s)^2 / 2\sigma_t) (\partial f_\theta(\mathbf{z}_s, \sigma_s) / \partial \sigma_s),
 \end{aligned} \quad (4)$$

where $t, s \in \{0, \dots, N\}$ and $1 \leq s < t \leq N$. Our derivation can be found in Appendix 9.7. The challenge of using Eq. 4 lies in performing addition/subtraction operations on the token maps at different time steps. We adopt a simple yet effective approach by transforming the operations into probability distributions and then performing token replacement based on these distributions. For instance, since $\frac{\sigma_t}{\sigma_s} + \left(-\frac{\sigma_t - \sigma_s}{\sigma_s}\right) = 1$, for the 1st order Solver, we select $100 \frac{\sigma_t}{\sigma_s} \%$ of the tokens from \mathbf{z}_s and $100 \frac{\sigma_s - \sigma_t}{\sigma_s} \%$ of the tokens from $f_\theta(\mathbf{z}_t, \sigma_t)$, and simply merge them.

For the token selection rule, we follow a high-confidence criterion, selecting the top $100 \frac{\sigma_s - \sigma_t}{\sigma_s} \%$ of tokens with the highest confidence from $f_\theta(\mathbf{z}_t, \sigma_t)$. Additionally, for the gradient in the 2nd order solver, we use the same difference expansion form as in DPM-Solver. We present the ablation

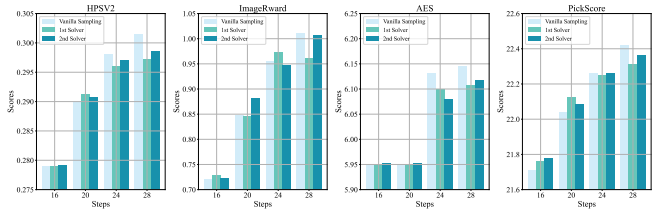


Figure 12. Ablation Studies of Momentum-based Solver.

experiments in Fig. 12, which reveals that the Momentum-based Solver provides performance gains for $N=16$ and $N=20$, but does not perform as well as vanilla sampling for larger N . We argue this is due to the discrete nature of the token values, which restricts the effectiveness of addition/subtraction operations, unlike in DM.

5. Challengebench and Additional Evaluations

We further analyze the performance of MGT on challenging prompts. We synthesize 150k images using SD XL [29], computed HPS v2 scores, and selected 1.5k prompts with the lowest scores. After manual and GPT-4o [1] selection, we form *Challengebench* with 220 semantically sound prompts. We conduct experiments using Meissonic, SD XL [29], FLUX.1-schnell [16], and SD-3.5-Large [40] on Challengebench, and present the results in Table 4. We observe that Meissonic’s improvement over SD XL on Challengebench ($0.1838 \rightarrow 0.2116$) was greater than its improvement on HPD v2 ($0.2888 \rightarrow 0.2957$) in Meissonic’s

original paper, suggesting that MGT is more robust on challenging prompts. The reduced scores of FLUX.1-schnell and SD-3.5-Large on Challengebench indicate that it provides a robust measure of generalization. *We achieve winning rates of approximately 70% using combination of design choices compared to vanilla sampling in Table 11. More experiments please see Appendix 9.9.*

6. Conclusion

Our approach with the masked generative transformer, aimed at ensuring enhanced and efficient inference, represents a meaningful exploration of non-autoregressive models. In future, we will try to unify and improve the training process of the masked generative transformer and overcome the bottlenecks of this generative paradigm.

References

- [1] Josh Achiam, Steven Adler, Sandhini Agarwal, Lama Ahmad, Ilge Akkaya, Florencia Leoni Aleman, Diogo Almeida, Janko Altenschmidt, Sam Altman, Shyamal Anadkat, et al. Gpt-4 technical report. *arXiv preprint arXiv:2303.08774*, 2023. 8
- [2] Anonymous. Zigzag diffusion sampling: The path to success is zigzag. In *Submitted to The Thirteenth International Conference on Learning Representations*, 2024. under review. 2, 4, 5
- [3] Jinbin Bai, Tian Ye, Wei Chow, Enxin Song, Qing-Guo Chen, Xiangtai Li, Zhen Dong, Lei Zhu, and Shuicheng Yan. Meissonic: Revitalizing masked generative transformers for efficient high-resolution text-to-image synthesis. *arXiv preprint arXiv:2410.08261*, 2024. 1, 3, 4
- [4] Daniel Bolya and Judy Hoffman. Token merging for fast stable diffusion. In *Proceedings of the IEEE/CVF conference on computer vision and pattern recognition*, pages 4599–4603, 2023. 2, 4, 7
- [5] Huiwen Chang, Han Zhang, Lu Jiang, Ce Liu, and William T Freeman. Maskgit: Masked generative image transformer. In *Proceedings of the IEEE/CVF Conference on Computer Vision and Pattern Recognition*, pages 11315–11325, 2022. 1, 3, 4
- [6] Huiwen Chang, Han Zhang, Jarred Barber, AJ Maschinot, Jose Lezama, Lu Jiang, Ming-Hsuan Yang, Kevin Murphy, William T Freeman, Michael Rubinstein, et al. Muse: Text-to-image generation via masked generative transformers. *arXiv preprint arXiv:2301.00704*, 2023. 1, 3
- [7] Lei Chen, Yuan Meng, Chen Tang, Xinzhu Ma, Jingyan Jiang, Xin Wang, Zhi Wang, and Wenwu Zhu. Q-dit: Accurate post-training quantization for diffusion transformers. *arXiv preprint arXiv:2406.17343*, 2024. 4
- [8] Lijie Fan, Tianhong Li, Siyang Qin, Yuanzhen Li, Chen Sun, Michael Rubinstein, Deqing Sun, Kaiming He, and Yonglong Tian. Fluid: Scaling autoregressive text-to-image generative models with continuous tokens. *arXiv preprint arXiv:2410.13863*, 2024. 1
- [9] Jack Hessel, Ari Holtzman, Maxwell Forbes, Ronan Le Bras, and Yejin Choi. Clipscore: A reference-free evaluation metric for image captioning, 2022. 1
- [10] Martin Heusel, Hubert Ramsauer, Thomas Unterthiner, Bernhard Nessler, and Sepp Hochreiter. Gans trained by a two time-scale update rule converge to a local nash equilibrium. In *Neural Information Processing Systems*, Long Beach Convention Center, Long Beach, 2017. NeurIPS. 3, 1
- [11] Jonathan Ho and Tim Salimans. Classifier-free diffusion guidance. In *Neural Information Processing Systems Workshop*, Virtual Event, 2021. NeurIPS. 4
- [12] Jonathan Ho, Ajay Jain, and Pieter Abbeel. Denoising diffusion probabilistic models. In *Neural Information Processing Systems*, pages 6840–6851, Virtual Event, 2020. NeurIPS. 1, 3, 4
- [13] Benoit Jacob, Skirmantas Kligys, Bo Chen, Menglong Zhu, Matthew Tang, Andrew Howard, Hartwig Adam, and Dmitry Kalenichenko. Quantization and training of neural networks for efficient integer-arithmetic-only inference. In *Proceedings of the IEEE conference on computer vision and pattern recognition*, pages 2704–2713, 2018. 7
- [14] Tero Karras, Miika Aittala, Timo Aila, and Samuli Laine. Elucidating the design space of diffusion-based generative models. *Advances in neural information processing systems*, 35:26565–26577, 2022. 2, 4
- [15] Diederik P Kingma. Auto-encoding variational bayes. *arXiv preprint arXiv:1312.6114*, 2013. 4
- [16] Black Forest Labs. Flux. <https://blackforestlabs.ai/>, 2024. 1, 7, 8
- [17] Laion.ai. Laion-aesthetics. <https://laion.ai/blog/laion-aesthetics/>, 2022. 3, 1
- [18] Sangyun Lee, Beomsu Kim, and Jong Chul Ye. Minimizing trajectory curvature of ode-based generative models. *arXiv preprint arXiv:2301.12003*, 2023. 4
- [19] Tsung-Yi Lin, Michael Maire, Serge Belongie, James Hays, Pietro Perona, Deva Ramanan, Piotr Dollár, and C Lawrence Zitnick. Microsoft coco: Common objects in context. In *European Conference on Computer Vision*, pages 740–755. Springer, 2014. 3, 1
- [20] Buhua Liu, Shitong Shao, Bao Li, Lichen Bai, Haoyi Xiong, James Kwok, Sumi Helal, and Zeke Xie. Alignment of diffusion models: Fundamentals, challenges, and future. *arXiv preprint arXiv:2409.07253*, 2024. 1
- [21] Dongyang Liu, Shitian Zhao, Le Zhuo, Weifeng Lin, Yu Qiao, Hongsheng Li, and Peng Gao. Lumina-mgpt: Illuminate flexible photorealistic text-to-image generation with multimodal generative pretraining. *arXiv preprint arXiv:2408.02657*, 2024. 1, 3
- [22] Xingchao Liu, Chengyue Gong, and Qiang Liu. Flow straight and fast: Learning to generate and transfer data with rectified flow. *arXiv preprint arXiv:2209.03003*, 2022. 4
- [23] Cheng Lu, Yuhao Zhou, Fan Bao, Jianfei Chen, and Chongxuan Li. Dpm-solver++: Fast solver for guided sampling of diffusion probabilistic models. *arXiv preprint arXiv:2211.01095*, 2022. 2, 7
- [24] Cheng Lu, Yuhao Zhou, Fan Bao, Jianfei Chen, Chongxuan Li, and Jun Zhu. Dpm-solver: A fast ode solver for diffusion

- probabilistic model sampling in around 10 steps. In *Neural Information Processing Systems*, New Orleans, LA, USA, 2022. NeurIPS. 2, 4, 7
- [25] Chenlin Meng, Ruiqi Gao, Diederik P Kingma, Stefano Ermon, Jonathan Ho, and Tim Salimans. On distillation of guided diffusion models. *arXiv preprint arXiv:2210.03142*, 2022. 5
- [26] Ron Mokady, Amir Hertz, Kfir Aberman, Yael Pritch, and Daniel Cohen-Or. Null-text inversion for editing real images using guided diffusion models. In *Proceedings of the IEEE/CVF Conference on Computer Vision and Pattern Recognition*, pages 6038–6047, 2023. 2
- [27] OpenAI. Learning to reason with llms, 2024. 1
- [28] William Peebles and Saining Xie. Scalable diffusion models with transformers. In *Proceedings of the IEEE/CVF International Conference on Computer Vision*, pages 4195–4205, 2023. 4
- [29] Dustin Podell, Zion English, Kyle Lacey, Andreas Blattmann, Tim Dockhorn, Jonas Müller, Joe Penna, and Robin Rombach. Sdxl: Improving latent diffusion models for high-resolution image synthesis. In *The Twelfth International Conference on Learning Representations*. 1, 3, 8
- [30] Zipeng Qi, Lichen Bai, Haoyi Xiong, et al. Not all noises are created equally: Diffusion noise selection and optimization. *arXiv preprint arXiv:2407.14041*, 2024. 7
- [31] Alec Radford, Jong Wook Kim, Chris Hallacy, Aditya Ramesh, Gabriel Goh, Sandhini Agarwal, Girish Sastry, Amanda Askell, Pamela Mishkin, Jack Clark, Gretchen Krueger, and Ilya Sutskever. Learning transferable visual models from natural language supervision, 2021. 1
- [32] Tim Salimans and Jonathan Ho. Progressive distillation for fast sampling of diffusion models. In *International Conference on Learning Representations*, Virtual Event, 2022. OpenReview.net. 7
- [33] Tim Salimans, Ian Goodfellow, Wojciech Zaremba, Vicki Cheung, Alec Radford, and Xi Chen. Improved techniques for training gans. In *Neural Information Processing Systems*, Centre Convencions Internacional Barcelona, Barcelona SPAIN, 2016. NeurIPS. 1
- [34] Rico Sennrich. Neural machine translation of rare words with subword units. *arXiv preprint arXiv:1508.07909*, 2015. 1
- [35] Shitong Shao, Xu Dai, Shouyi Yin, Lujun Li, Huanran Chen, and Yang Hu. Catch-up distillation: You only need to train once for accelerating sampling. *arXiv preprint arXiv:2305.10769*, 2023. 1
- [36] Shitong Shao, Xiaohan Yuan, Zhen Huang, Ziming Qiu, Shuai Wang, and Kevin Zhou. Diffuseexpand: Expanding dataset for 2d medical image segmentation using diffusion models. *arXiv preprint arXiv:2304.13416*, 2023.
- [37] Jiaming Song, Chenlin Meng, and Stefano Ermon. Denoising diffusion implicit models. In *International Conference on Learning Representations*, kigali, rwanda, 2023. OpenReview.net. 1, 4, 7
- [38] Yang Song, Prafulla Dhariwal, Mark Chen, and Ilya Sutskever. Consistency models. *arXiv preprint arXiv:2303.01469*, 2023. 7
- [39] Yang Song, Jascha Sohl-Dickstein, Diederik P Kingma, Abhishek Kumar, Stefano Ermon, and Ben Poole. Score-based generative modeling through stochastic differential equations. In *International Conference on Learning Representations*, kigali, rwanda, 2023. OpenReview.net. 1, 4
- [40] Stability.ai. Introducing stable diffusion 3.5. <https://stability.ai/news/introducing-stable-diffusion-3-5>, 2024. 7, 8
- [41] Jianlin Su, Murtadha Ahmed, Yu Lu, Shengfeng Pan, Wen Bo, and Yunfeng Liu. Roformer: Enhanced transformer with rotary position embedding. *Neurocomputing*, 568:127063, 2024. 7
- [42] Peize Sun, Yi Jiang, Shoufa Chen, Shilong Zhang, Bingyue Peng, Ping Luo, and Zehuan Yuan. Autoregressive model beats diffusion: Llama for scalable image generation. *arXiv preprint arXiv:2406.06525*, 2024. 1, 3, 4
- [43] Gemma Team, Thomas Mesnard, Cassidy Hardin, Robert Dadashi, Surya Bhupatiraju, Shreya Pathak, Laurent Sifre, Morgane Rivière, Mihir Sanjay Kale, Juliette Love, et al. Gemma: Open models based on gemini research and technology. *arXiv preprint arXiv:2403.08295*, 2024. 1
- [44] Yao Teng, Han Shi, Xian Liu, Xuefei Ning, Guohao Dai, Yu Wang, Zhenguo Li, and Xihui Liu. Accelerating autoregressive text-to-image generation with training-free speculative jacobi decoding. *arXiv preprint arXiv:2410.01699*, 2024. 1
- [45] Yao Teng, Han Shi, Xian Liu, Xuefei Ning, Guohao Dai, Yu Wang, Zhenguo Li, and Xihui Liu. Accelerating autoregressive text-to-image generation with training-free speculative jacobi decoding. *arXiv preprint arXiv:2410.01699*, 2024. 4
- [46] Hugo Touvron, Thibaut Lavril, Gautier Izacard, Xavier Martinet, Marie-Anne Lachaux, Timothée Lacroix, Baptiste Rozière, Naman Goyal, Eric Hambro, Faisal Azhar, et al. Llama: Open and efficient foundation language models. *arXiv preprint arXiv:2302.13971*, 2023. 1
- [47] Aaron Van Den Oord, Oriol Vinyals, et al. Neural discrete representation learning. *Advances in neural information processing systems*, 30, 2017. 4
- [48] Xiaoshi Wu, Yiming Hao, Keqiang Sun, Yixiong Chen, Feng Zhu, Rui Zhao, and Hongsheng Li. Human preference score v2: A solid benchmark for evaluating human preferences of text-to-image synthesis, 2023. 3, 1
- [49] Xiaoshi Wu, Yiming Hao, Keqiang Sun, Yixiong Chen, Feng Zhu, Rui Zhao, and Hongsheng Li. Human preference score v2: A solid benchmark for evaluating human preferences of text-to-image synthesis. *arXiv preprint arXiv:2306.09341*, 2023. 1
- [50] Jiazheng Xu, Xiao Liu, Yuchen Wu, Yuxuan Tong, Qinkai Li, Ming Ding, Jie Tang, and Yuxiao Dong. Imagereward: Learning and evaluating human preferences for text-to-image generation, 2023. 3, 1
- [51] Qinsheng Zhang and Yongxin Chen. Fast sampling of diffusion models with exponential integrator. In *International Conference on Learning Representations*. OpenReview.net, 2023. 4

- [52] Hengshuang Zhao, Jiaya Jia, and Vladlen Koltun. Exploring self-attention for image recognition. In *Computer Vision and Pattern Recognition*, pages 10076–10085, 2020. [1](#)
- [53] Kaiwen Zheng, Cheng Lu, Jianfei Chen, and Jun Zhu. Dpm-solver-v3: Improved diffusion ode solver with empirical model statistics. *Advances in Neural Information Processing Systems*, 36:55502–55542, 2023. [7](#)

Bag of Design Choices for Inference of High-Resolution Masked Generative Transformer

Supplementary Material

7. Benchmark and Evaluation Metrics

In this section, we provide an overview of the benchmarks, evaluation metrics, and related content used in our main paper.

7.1. Benchmark

HPD v2. The Human Preference Dataset v2 [48] is a large-scale dataset with clean annotations that focuses on user preferences for images synthesized from text prompts. It consists of 798,090 binary preference choices across 433,760 image pairs, designed to address the shortcomings of existing evaluation metrics that do not accurately capture human preferences. In line with the methodologies outlined in [3, 48], we utilized four subsets for our review: Animation, Concept-art, Painting, and Photo, with each subset containing 800 prompts.

HPD v2 Subset. In order to reduce the evaluation computational overhead, we randomly selected 150 prompts from HPD V2 [48] to build a new collection of prompts for evaluation.

Challengebench. As detailed in Sec. 5, we initially generated 150,000 images using SD XL Base v1.0. We then filtered out the lowest-performing 1,500 prompts based on HPS v2 metrics. Finally, through a combination of manual filtering and GPT-4o filtering, we arrived at a final set of 220 semantically correct and complete prompts.

7.2. Evaluation Metrics

PickScore. PickScore is a scoring function based on the CLIP model, developed using the Pick-a-Pic dataset, which gathers user preferences for generated images. This method demonstrates performance that exceeds typical human benchmarks in predicting user preferences. By effectively aligning with human evaluations and utilizing the diverse distribution prompts from Pick-a-Pic, PickScore facilitates a more pertinent assessment of text-to-image models compared to conventional metrics like FID [10] on datasets such as MS-COCO [19].

HPS v2. The Human preference score version 2 (HPS v2) represents a refined model for predicting user preferences, achieved through fine-tuning the CLIP framework [31] on the human preference dataset version 2. This model is designed to align text-to-image generation with user tastes by

estimating the likelihood that a generated image will be favored by individuals, thereby serving as a robust tool for evaluating the efficacy of text-to-image models across varied image distributions.

AES. The Aesthetic score (AES) [17] is computed using a model built on CLIP embeddings, enhanced with additional multilayer perceptron (MLP) layers to quantify the visual appeal of images. This metric is useful for assessing the aesthetic quality of generated images, offering insights into their alignment with human aesthetic preferences.

ImageReward. ImageReward [50] is a specialized reward model focused on evaluating text-to-image synthesis through human preferences. It is trained on a substantial dataset comprising human comparisons, enabling it to effectively capture user inclinations. The model evaluates synthesized images based on several factors, including their correspondence to the text prompt and overall aesthetic merit. ImageReward has demonstrated superior performance over traditional metrics such as the Inception Score (IS) [33] and Fréchet Inception Distance (FID) in reflecting human judgments, positioning it as a promising automatic evaluation tool for text-to-image synthesis.

CLIPScore. CLIPScore [9] utilizes the strengths of the CLIP model, which integrates images and text within a shared embedding space. By measuring the cosine similarity between image and text embeddings, CLIPScore provides an evaluation of how closely a generated image aligns with its textual description. Although effective in assessing text-image correlation, CLIPScore may not fully capture the subtleties of human preferences, especially regarding aesthetic qualities and intricate details.

8. Ineffective Method

Here, we summarize a collection of algorithms that demonstrate limited effectiveness when applied to MGT, aiming to provide valuable insights for other researchers.

8.1. Deterministic Sampling

Deterministic sampling techniques, such as DDIM [37], have been developed for DMs to facilitate tasks like image editing and accelerated sampling. Consequently, we are interested in exploring whether MGT can be adapted for deterministic sampling. In our investigation, we identified



Figure 13. The visualization of deterministic sampling, where the number following deterministic sampling indicates the step from which `torch.argmax` is used in place of `torch.multinomial`, results in outputs that do not exhibit significant perceptual quality degradation. Despite the lack of noticeable decline in visual fidelity, this shift adversely affects the quantitative metrics.

Method	HPS v2 (↑)	ImageReward (↑)	AES (↑)	PickScore (↑)
Vanilla	0.3062	1.0627	6.1938	22.5037
Deter. Sampling (60-64)	0.3061	1.0619	6.1983	22.4872
Deter. Sampling (56-64)	0.3056	1.0664	6.1925	22.4618
Deter. Sampling (52-64)	0.3057	1.0498	6.1832	22.4627
Deter. Sampling (48-64)	0.3055	1.0679	6.1823	22.4574
Deter. Sampling (44-64)	0.3048	1.0545	6.1926	22.4675
Deter. Sampling (40-64)	0.3047	1.0676	6.1941	22.4355
Deter. Sampling (36-64)	0.3051	1.0654	6.2043	22.4516
Deter. Sampling (30-64)	0.3043	1.0514	6.1864	22.4204

Table 6. Quantitative comparison between vanilla sampling and deterministic sampling (Deter. Sampling).

two stochastic elements within the sampling mechanism of MGT: first, the process of determining which regions of the subsequent sample should be masked; second, the sampling procedure defined by $\arg \max_i \frac{\log(\epsilon)}{\mathbf{p}}$, where \mathbf{p} represents the logit and ϵ is drawn from a uniform distribution $\mathcal{U}[0, 1]$. We find that eliminating randomness in the former causes the sampling pipeline to collapse. In the latter, randomness can only be reduced during the later stages of sampling (*i.e.*, when t approaches 1); otherwise, the sampling quality deteriorates significantly.

Table 6 presents the results, showing that the introduction of deterministic sampling does not lead to significant metric improvements but instead results in performance degradation. Consequently, we do not consider it a valid technique.

9. Additional Information of Effective Method

Here, we present discussions, analyses, and experimental results that could not be developed due to space limitations in the main paper.

9.1. Additional Experiments of Different Noise Schedule

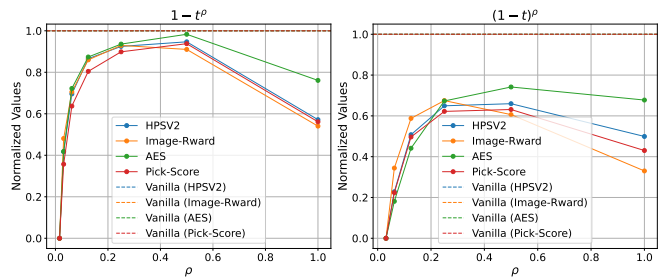


Figure 14. Visualization of the performance of different noise schedules. The dotted line denotes the vanilla sampling, and N is set to 48.

As a supplement to Sec. 3.1, we present the experimental results for the number of sampling steps $N = 48$ and $N = 32$, conducted on the HPD v2 Subset, in Figs 14 and 15, respectively. We further tested the performance of the noise schedule $1 - t^{0.6}$ at $N = 64$ on the full HPD

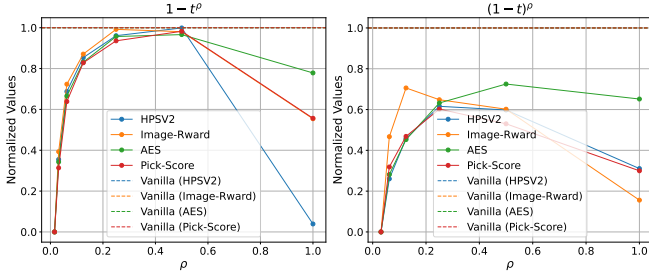


Figure 15. Visualization of the performance of different noise schedules. The dotted line denotes the vanilla sampling, and N is set to 32.

Subset of HPD v2	Method	HPS v2 (\uparrow)	ImageReward (\uparrow)	AES (\uparrow)	PickScore (\uparrow)
Anime	$\cos(\frac{\pi}{2})$	0.3053	0.9577	6.1049	22.4776
Anime	$1 - t^{0.6}$	0.3099	1.0697	6.1068	22.6601
Photo	$\cos(\frac{\pi}{2})$	0.2658	0.5161	5.9992	21.5552
Photo	$1 - t^{0.6}$	0.2712	0.6011	5.9894	21.6501
Paintings	$\cos(\frac{\pi}{2})$	0.2915	1.0802	6.4790	21.8669
Paintings	$1 - t^{0.6}$	0.2907	1.0911	6.4501	21.9569
Concept-Art	$\cos(\frac{\pi}{2})$	0.2928	1.0219	6.3508	21.8251
Concept-Art	$1 - t^{0.6}$	0.2937	1.0238	6.3602	21.8232

Table 7. Quantitative comparison between cosine schedule and $1 - t^{0.6}$ on the HPD v2.

Method	PickScore (\uparrow)	HPS v2 (\uparrow)	AES (\uparrow)	ImageReward (\uparrow)	CLIPScore (\uparrow)
Vanilla Sampling	22.5034	0.30566	6.2038	1.0523	0.8378
Z-Sampling (8)	22.4932	0.30476	6.1949	1.0344	0.8398
Z-Sampling (16)	22.4295	0.27625	6.1669	1.0133	0.8317
Z-Sampling (32)	22.0241	0.29795	6.0329	0.8596	0.8185
Z-Sampling (48)	21.3509	0.30499	5.7563	0.6134	0.8025
Z-Sampling (64)	18.1041	0.11721	4.0962	-2.0106	0.6003

Table 8. The experimental result of Z-Sampling using the random masking mechanism.

v2 benchmark and presented the result in Table 7. Table 7 shows that $1 - t^{0.6}$ outperforms $\cos(\frac{\pi t}{2})$ on the vast majority of metrics and subsets within the HPD v2, despite the potential risk of overfitting introduced by this exhaustive search approach on the hyperparameter ρ .

9.2. Exploration of Z-Sampling

In this subsection we focus on showing some experimental results of Z-Sampling as a complement to the main paper.

The results in Table 8 are obtained using the random masking mechanism (*i.e.*, vanilla Z-Sampling in Fig. 5), with the numbers in parentheses indicating the total number of Z-Sampling operations performed from the 0th step. It can be observed that this approach generally impairs the inference performance of the MGT.

We also designed another masking algorithm named recover Z-sampling, which directly reuses the mask from the first sampling from the $(i - 1)$ th step to the i th step. The results of vanilla sampling, this algorithm and masked Z-Sampling are presented in Table 9, where we find that this approach also yields significant performance gains, similar to masked Z-Sampling. It should be noted that, unless oth-

Sampling Step N	Method	PickScore (\uparrow)	HPS v2 (\uparrow)	AES (\uparrow)	ImageReward (\uparrow)
16	Vanilla Sampling	21.7214	0.2792	5.9680	0.7154
	Recover Z-Sampling	21.9711	0.2853	6.0249	0.8400
	Masked Z-Sampling	22.2514	0.3016	6.1017	0.8901
48	Vanilla Sampling	22.4894	0.3048	6.2157	1.0804
	Recover Z-Sampling	22.4380	0.3041	6.1774	1.0242
	Masked Z-Sampling	22.5826	0.3110	6.2198	1.0918
64	Vanilla Sampling	22.5034	0.3056	6.2038	1.0523
	Recover Z-Sampling	22.4747	0.3064	6.2296	1.0838
	Masked Z-Sampling	22.5375	0.3087	6.1769	1.0559

Table 9. Comparison of vanilla sampling, masked Z-Sampling and recover Z-Sampling on the HPD v2 Subset.

erwise specified, all experiments in this paper are conducted using masked Z-Sampling.

9.3. Comparison of Noise Regularization

Dataset	Method	PickScore (\uparrow)	HPS v2 (\uparrow)	AES (\uparrow)	ImageReward (\uparrow)
Anime	Vanilla Sampling	22.4776	0.3053	6.1049	0.9577
	Noise Regularization	22.6988	0.3133	6.1262	1.1107
Concept-art	Vanilla Sampling	21.8251	0.2928	6.3509	1.0219
	Noise Regularization	21.8862	0.2951	6.3844	1.0492
Photo	Vanilla Sampling	21.5552	0.2658	5.9993	0.5161
	Noise Regularization	21.6358	0.2691	6.0055	0.6005
Paintings	Vanilla Sampling	21.8669	0.2915	6.4791	1.0802
	Noise Regularization	21.9340	0.2928	6.4997	1.1013

Table 10. Comparison of vanilla sampling and noise regularization on HPD v2.

We present the results of the comparative experiments on noise regularization in Table 10, which show that it outperforms vanilla sampling across all domains and metrics.

9.4. Comparison of Differential Sampling

Dataset	Method	PickScore (\uparrow)	HPSV2 (\uparrow)	AES (\uparrow)	ImageReward (\uparrow)
Anime	Vanilla Sampling	22.4776	0.3053	6.1049	0.9577
	Differential Sampling	22.6472	0.3108	6.1050	1.0796
Photo	Vanilla Sampling	21.5552	0.2658	5.9992	0.5161
	Differential Sampling	21.6730	0.2700	6.0203	0.6067
Paintings	Vanilla Sampling	21.8669	0.2915	6.4790	1.0802
	Differential Sampling	21.9769	0.2917	6.4592	1.0944
Concept-Art	Vanilla Sampling	21.8251	0.2928	6.3508	1.0219
	Differential Sampling	21.8630	0.2951	6.3659	1.0493

Table 11. Comparison of vanilla sampling and differential sampling on HPD v2.

Similar to Sec. 9.3, we present the results of the comparative experiments on differential sampling in Table 11. On HPD v2, a large-scale benchmark consisting of 3,200 prompts, differential sampling outperforms vanilla sampling across nearly all metrics and domains.

9.5. Detail Implementation of Token Merging on RoPE

Here, we describe how to perform token merging on RoPE. Assume that tokens can be defined as $\{\mathbf{n}_i\}_{i=1}^N$, then the self-

attention can be expressed as

$$\begin{aligned}
q_i &= f_q(\mathbf{n}_i, i), \\
k_j &= f_k(\mathbf{n}_j, j), \\
v_j &= f_v(\mathbf{n}_j, j), \\
a_{i,j} &= \frac{\exp(\frac{q_i^T k_j}{\sqrt{d}})}{\sum_{k=1}^N \exp(\frac{q_i^T k_k}{\sqrt{d}})} \\
\mathbf{o}_j &= \sum_{i=1}^N a_{i,j} v_i,
\end{aligned} \tag{5}$$

where N and d denote the number of tokens and the length of each token, respectively. The core of RoPE is to inject positional information into the computations involving $f_q(\cdot, \cdot)$ and $f_k(\cdot, \cdot)$, the key lies in the matrix Q_j^d :

$$Q_j^d = \begin{pmatrix} \cos(j\theta_0) & -\sin(j\theta_0) & \cdots & 0 & 0 \\ \sin(j\theta_0) & \cos(j\theta_0) & \cdots & 0 & 0 \\ 0 & 0 & \cdots & 0 & 0 \\ \vdots & \vdots & \ddots & \vdots & \vdots \\ 0 & 0 & \cdots & \cos(j\theta_{\frac{d}{2}-1}) & -\sin(j\theta_{\frac{d}{2}-1}) \\ 0 & 0 & \cdots & \sin(j\theta_{\frac{d}{2}-1}) & \cos(j\theta_{\frac{d}{2}-1}) \end{pmatrix}, \tag{6}$$

where $\theta_i = 10000^{-2(i-1)/d}$ and $i \in [1, 2, \dots, d/2]$. The functions $f_q(\cdot, \cdot)$ and $f_k(\cdot, \cdot)$ can then be expressed as

$$\begin{aligned}
f_q(\mathbf{n}_j, j) &= Q_j^d W_q \mathbf{n}_j, \\
f_k(\mathbf{n}_j, j) &= Q_j^d W_k \mathbf{n}_j.
\end{aligned} \tag{7}$$

TomeMGT first computes a similarity matrix between tokens to determine which highly similar tokens should be merged. For the tokens identified for merging, their mean value is calculated to obtain the merged tokens. Given the tokens \mathbf{n}_i and \mathbf{n}_j that need to be merged, their merged token can be obtained as $\mathbf{n}_{i+j} = \frac{\mathbf{n}_i + \mathbf{n}_j}{2}$. We found it effective to apply the same strategy for RoPE, specifically, $Q_{i+j}^d = \frac{Q_i^d + Q_j^d}{2}$. It is worth noting that we also tried using Q_{i+j}^d directly as either Q_i^d or Q_j^d , but this approach led to inference collapse.

9.6. Comparison of TomeMGT

Dataset	Method	HPS v2 (↑)	ImageReward (↑)	AES (↑)	PickScore (↑)
Anime	Vanilla Sampling	0.3053	0.9577	6.1049	22.4776
	TomeMGT	0.2866	0.7919	5.8713	21.8028
Photo	Vanilla Sampling	0.2658	0.5161	5.9992	21.5552
	TomeMGT	0.2430	0.1883	5.7982	20.8134
Paintings	Vanilla Sampling	0.2915	1.0802	6.4790	21.8669
	TomeMGT	0.2736	0.7780	6.1859	21.0760
Concept-Art	Vanilla Sampling	0.2928	1.0219	6.3508	21.8251
	TomeMGT	0.2757	0.7658	6.0891	21.0819

Table 12. Comparison between TomeMGT and vanilla sampling.

Here, we provide the experimental results of our proposed TomeMGT on HPD v2, as shown in Table 12. The

merging ratio is set to 0.5 for all experiments. It can be observed that TomeMGT does not perform as well compared to our proposed methods: noise regularization, differential sampling, masked Z-Sampling, and SCQ. However, this algorithm may hold significant potential if the parameter size and number of tokens in MGT are further increased in the future.

9.7. Derivation of Momentum-based Solver

The original derivation of DPM-Solver was based on the DM paradigm, not MGT. However, DPM-Solver is theoretically adaptable to DMs with any noise schedule, which suggests the potential for its application to MGT. While MGT uses a cosine schedule as the default noise schedule, other forms, such as the Karras-like schedule introduced in this paper [14], can also be applied. The crucial requirement in MGT is that $\alpha_t + \sigma_t = 1$, since the number of masked tokens and the number of unmasked tokens must together equal the total number of tokens. Given this, we first derive the DPM-Solver for predicting \mathbf{z}_N scenarios based on the flow matching paradigm [18, 22], and then substitute the corresponding noise schedule. The flow matching can be written as

$$\frac{d\mathbf{z}_t}{dt} = -\mathbf{v}_\theta(\mathbf{z}_t, t). \tag{8}$$

For simplicity, we assume t is continuous and $t \in [0, 1]$, where \mathbf{z}_1 corresponds to the original \mathbf{z}_N and \mathbf{z}_0 to the original \mathbf{z}_0 . Let $\mathbf{v}_\theta(\mathbf{z}_t, t)$ denote the model for estimating $\mathbf{z}_0 - \mathbf{z}_N$. Substituting in the prediction target \mathbf{z}_N , we can obtain

$$\begin{aligned}
\frac{d\mathbf{z}_t}{dt} &= -\frac{\mathbf{z}_t - f_\theta(\mathbf{z}_t, t)}{t}, \\
\implies \frac{d\mathbf{z}_t}{dt} &= \frac{-1}{t} \mathbf{z}_t + \frac{1}{t} f_\theta(\mathbf{z}_t, t),
\end{aligned} \tag{9}$$

where $f_\theta(\mathbf{z}_t, t)$ stands for the backbone (*i.e.*, Transformer) of MGT. Calculate the analytical solution of a partial differential equation over a specified interval $[s, t]$ ($0 \leq s < t \leq 1$):

$$\begin{aligned}
\mathbf{z}_t &= e^{\int_s^t \frac{-1}{\tau} d\tau} \mathbf{z}_s + \int_s^t \left(e^{\int_\tau^t \frac{-1}{r} dr} \left(\frac{1}{\tau} f_\theta(\mathbf{z}_\tau, \tau) \right) \right) d\tau, \\
\implies \mathbf{z}_t &= \left(\frac{s}{t} \right) \mathbf{z}_s + \int_s^t \left(\left[\frac{1}{t} \right] f_\theta(\mathbf{z}_\tau, \tau) \right) d\tau.
\end{aligned} \tag{10}$$

Let $f_\theta(\mathbf{z}_\tau, \tau)$ be Taylor-expanded at s , we can obtain:

$$\mathbf{z}_t = \frac{s}{t} \mathbf{z}_s + \int_s^t \left(\left[\frac{1}{t} \right] \left[f_\theta(\mathbf{z}_s, s) + (\tau - s) \frac{\partial f_\theta(\mathbf{z}_s, s)}{\partial s} \right] \right) d\tau. \tag{11}$$

In this paper, we consider only second-order Taylor expansions. From this, we derive the first-order and second-order expressions for the Momentum-based Solver:

$$\begin{aligned} \mathbf{z}_t &= \frac{s}{t} \mathbf{z}_s + \frac{t-s}{t} f_\theta(\mathbf{z}_s, s), \text{ \# 1st order} \\ \mathbf{z}_t &= \frac{s}{t} \mathbf{z}_s + \frac{t-s}{t} f_\theta(\mathbf{z}_s, s) \text{ \# 2nd order} \\ &+ \frac{(t-s)^2}{2t} \frac{\partial f_\theta(\mathbf{z}_s, s)}{\partial s}. \end{aligned} \quad (12)$$

Substitute σ_s and σ_t into Eq. 12:

$$\begin{aligned} \mathbf{z}_t &= \frac{\sigma_s}{\sigma_t} \mathbf{z}_s + \frac{\sigma_t - \sigma_s}{\sigma_t} f_\theta(\mathbf{z}_s, \sigma_s), \text{ \# 1st order} \\ \mathbf{z}_t &= \frac{\sigma_s}{\sigma_t} \mathbf{z}_s + \frac{\sigma_t - \sigma_s}{\sigma_t} f_\theta(\mathbf{z}_s, \sigma_s) \text{ \# 2nd order} \\ &+ \frac{(\sigma_t - \sigma_s)^2}{2\sigma_t} \frac{\partial f_\theta(\mathbf{z}_s, \sigma_s)}{\partial \sigma_s}. \end{aligned} \quad (13)$$

9.8. Additional Experiments on Challengebench

Due to space limitations in the main text, we present the experiments on Challengebench related to our proposed strategy in Table 15. From Table 15, it can be concluded that all of our strategies are effective.

9.9. Verification of Combinations of Algorithms

Due to space limitations in the main paper, we provide here a combination of design choices from Meissonic-512×512 and Meissonic-1024×1024 for the experiments. As illustrated in Table 13 and Table 14 (values in parentheses represent the winning rate of the combined design choice compared to vanilla sampling), it can be observed that these design choices, when combined, produce a synergistic effect greater than the sum of their individual contributions.

Dataset	Noise Regularization	Differential Sampling	Masked Z-Sampling	PickScore (\uparrow)	HPS v2 (\uparrow)	AES (\uparrow)	ImageReward (\uparrow)
Anime	✓		✓	22.5610	0.3139	5.9191	1.1811
				22.5734 (53%)	0.3152 (51%)	5.9066 (47%)	1.1779 (50%)
				22.6275 (56%)	0.3157 (52%)	5.9381 (56%)	1.1967 (54%)
				22.6528 (59%)	0.3175 (56%)	5.9169 (50%)	1.1994 (51%)
Photo	✓		✓	21.6864	0.2762	5.8391	0.6886
				21.7291 (53%)	0.2789 (53%)	5.8550 (52%)	0.7278 (52%)
				21.7558 (54%)	0.2815 (59%)	5.8782 (56%)	0.7974 (58%)
				21.7528 (54%)	0.2792 (56%)	5.8741 (53%)	0.7937 (57%)
Concept-art	✓		✓	21.7960	0.2949	6.2479	1.1199
				21.8513 (52%)	0.2979 (56%)	6.2383 (47%)	1.1274 (50%)
				21.8882 (59%)	0.2982 (60%)	6.2554 (51%)	1.1401 (54%)
				21.9483 (62%)	0.3013 (62%)	6.2370 (50%)	1.1545 (52%)
Paintings	✓		✓	21.8358	0.2924	6.3968	1.1747
				21.8839 (52%)	0.2941 (55%)	6.3992 (49%)	1.1855 (50%)
				21.9344 (57%)	0.2954 (58%)	6.3914 (50%)	1.1839 (53%)
				21.9621 (60%)	0.2959 (59%)	6.4006 (51%)	1.1728 (50%)

Table 13. Comparison of combination of different design choices with Meisssonc-512 \times 512 on HPD v2.

Dataset	Noise Regularization	Differential Sampling	Masked Z-Sampling	PickScore (\uparrow)	HPS v2 (\uparrow)	AES (\uparrow)	ImageReward (\uparrow)
Anime	✓		✓	22.6988 (58%)	0.3134 (56%)	6.1262 (52%)	1.1107 (55%)
				22.7559 (61%)	0.3184 (68%)	6.1165 (51%)	1.1175 (57%)
				22.8144 (65%)	0.3199 (69%)	6.1364 (55%)	1.1343 (58%)
				22.8115 (65%)	0.3203 (73%)	6.1375 (55%)	1.1130 (56%)
Concept-art	✓		✓	22.7559 (60%)	0.3184 (68%)	6.1165 (51%)	1.1175 (57%)
				21.8862 (55%)	0.2951 (54%)	6.3844 (57%)	1.0492 (52%)
				21.9617 (59%)	0.2996 (65%)	6.3679 (51%)	1.0611 (55%)
				22.0411 (65%)	0.3032 (71%)	6.4027 (57%)	1.0687 (55%)
Photo	✓		✓	22.0112 (64%)	0.3024 (70%)	6.3857 (55%)	1.0720 (67%)
				21.9617 (59%)	0.2996 (65%)	6.3679 (51%)	1.0611 (55%)
				21.6358 (54%)	0.2692 (55%)	6.0056 (51%)	0.6005 (53%)
				21.6628 (55%)	0.2747 (65%)	6.0728 (60%)	0.6307 (58%)
Paintings	✓		✓	21.7010 (59%)	0.2768 (69%)	6.0898 (61%)	0.6897 (60%)
				21.6634 (58%)	0.2753 (67%)	6.0805 (62%)	0.6427 (57%)
				21.6628 (55%)	0.2747 (65%)	6.0728 (60%)	0.6307 (58%)
				21.9340 (55%)	0.2928 (52%)	6.4998 (55%)	1.1013 (52%)
Paintings	✓		✓	22.0255 (62%)	0.2977 (62%)	6.5036 (54%)	1.1193 (53%)
				22.0595 (64%)	0.2995 (69%)	6.5164 (58%)	1.1249 (55%)
				22.0619 (60%)	0.2989 (67%)	6.4808 (52%)	1.1067 (55%)
				22.0255 (62%)	0.2977 (62%)	6.5036 (54%)	1.1193 (53%)

Table 14. Comparison of combination of different design choices with Meisssonc-1024 \times 1024 on HPD v2.

Model	Method	HPS v2 (\uparrow)	ImageReward (\uparrow)	AES (\uparrow)	PickScore (\uparrow)
Meisssonc	Vanilla Sampling	0.2116	0.0670	5.8503	19.3237
Meisssonc	Differential Sampling	0.2135	0.1114	5.8957	19.3381
Meisssonc	Our Noise Schedule	0.2120	0.0473	5.8635	19.3147
Meisssonc	Masked Z-Sampling	0.2183	0.1436	5.8885	19.3926
Meisssonc	Noise Regularization	0.2128	0.0748	5.8888	19.3645
Meisssonc	TokenMGT ($z\%=50\%$)	0.2000	-0.2593	5.5003	18.9691
Meisssonc	SCQ (W4A8)	0.2114	0.0590	5.8431	19.3365
SD XL	N/A	0.1838	-0.4915	5.8195	19.5792
FLUX.1-schnell (quant 8bit)	N/A	0.2257	0.2595	6.0357	19.6465
SD-3.5-Large (quant 4bit)	N/A	0.2114	0.0373	6.0848	19.7922

Table 15. Comparison of various models and methods on Challengebench.